Chemical Science

ROYAL SOCIETY OF CHEMISTRY

EDGE ARTICLE

View Article Online
View Journal | View Issue

Cite this: *Chem. Sci.*, 2022, **13**, 6967

All publication charges for this article have been paid for by the Royal Society of Chemistry

Oxygen-supplied mesoporous carbon nanoparticles for enhanced photothermal/photodynamic synergetic therapy against antibiotic-resistant bacterial infections†

Jiamei Zhou,[a] Wenjie Wang,[b] Qiuyang Zhang,[a] Zijun Zhang,[a] Jiangna Guo*[a] and Feng Yan *[a]

Pandemic and epidemic spread of antibiotic-resistant bacterial infections would result in a huge number of fatalities globally. To combat antibiotic-resistant pathogens, new antimicrobial strategies should be explored and developed to confront bacteria without acquiring or increasing drug-resistance. Here, oxygen saturated perfluorohexane (PFH)-loaded mesoporous carbon nanoparticles (CIL@ICG/PFH@O_2) with photothermal therapy (PTT) and enhanced photodynamic therapy (PDT) utility are developed for antibacterial applications. Ionic liquid groups are grafted onto the surface of mesoporous carbon nanoparticles, followed by anion-exchange with the anionic photosensitizer indocyanine green (ICG) and loading oxygen saturated PFH to prepare CIL@ICG/PFH@O_2. These CIL@ICG/PFH@O_2 nanoparticles exhibit effective PTT and enhanced PDT properties simultaneously upon 808 nm light irradiation. *In vitro* assays demonstrate that CIL@ICG/PFH@O_2 shows a synergistic antibacterial action against antibiotic-resistant pathogens (methicillin-resistant *Staphylococcus aureus* and kanamycin-resistant *Escherichia coli*). Moreover, CIL@ICG/PFH@O_2 could effectively kill drug-resistant bacteria *in vivo* to relieve inflammation and eliminate methicillin-resistant *Staphylococcus aureus*-wound infection under NIR irradiation, and the released oxygen can increase collagen deposition, epithelial tissue formation and blood vessel formation to promote wound healing while enhancing the PDT effect. This study proposes a platform with enhanced PTT/PDT effects for effective, controlled, and precise treatment of topical drug-resistant bacterial infections.

Received 25th March 2022
Accepted 16th May 2022

DOI: 10.1039/d2sc01740g

rsc.li/chemical-science

Introduction

Bacterial infections, particularly those caused by antibiotic-resistant bacteria, have resulted in significant morbidity and mortality.[1–3] The discovery of penicillin in 1928 and its mass production in the 1940s ushered in the "golden age" of antibiotics, which saved countless lives.[4–6] However, due to the widespread use and abuse of antibiotics, antibiotic-resistance has emerged at an alarming rate throughout the globe, making antibiotic-resistant bacteria a global concern in the 21st century. Antibiotic-resistant bacteria are a major cause of health-related morbidity and mortality, and human beings have ushered in the "post-antibiotic era".[7–9] Therefore, focusing on developing treatments to overcome pathogenic bacteria quickly and effectively without producing drug resistance is required.

Phototherapy, including photothermal therapy (PTT) and photodynamic therapy (PDT), has recently been identified as an effective antibacterial approach and has gained increased interest in antibacterial therapy.[10–15] In comparison to other treatment modalities, phototherapy offers distinct benefits due to its controllability, non-invasive nature, and few side effects. It has been reported that near-infrared (NIR) light with a wavelength of 700–1400 nm possesses a good ability to penetrate biological tissue while causing minimal damage to normal tissue.[16–18] PTT typically relies on NIR to irradiate photothermal agents to convert light energy into heat energy, which can destroy cell membranes and denature bacterial proteins, leading to bacterial death.[19,20] However, single-mode PTT is typically performed using high-power density NIR lasers and long-term exposure, showing limited therapeutic efficacy and safety with the potential to damage normal tissue.[21,22] Therefore, a combination of PTT and other therapies, such as PDT, is considered a better approach for eradicating bacteria, because it overcomes the limitations of a single therapy.[23–25]

[a]*Jiangsu Engineering Laboratory of Novel Functional Polymeric Materials, College of Chemistry, Chemical Engineering and Materials Science, Soochow University, Suzhou, 215123, China. E-mail: guojn@suda.edu.cn; fyan@suda.edu.cn*

[b]*Hematology Center, Cyrus Tang Medical Institute, Soochow University, Suzhou, 215123, China*

† Electronic supplementary information (ESI) available: Experimental section, N_2 desorption–adsorption isotherms, FTIR spectra, colony plate photographs, antibacterial data, and temperature curve. See https://doi.org/10.1039/d2sc01740g

PDT is based on photosensitizers (PSs) excited by specific wavelengths of light to transfer energy to oxygen molecules and generate cytotoxic reactive oxygen species (ROS): hydroxyl radical ($^{\bullet}OH$), superoxide anion ($O_2^{\bullet-}$), hydrogen peroxide (H_2O_2), and singlet oxygen ($^1O_2$).[26,27] ROS can oxidize and destroy biomolecules, such as lipids, proteins, and nucleic acids to induce cell apoptosis.[28] Among all kinds of PS, indocyanine green (ICG) is the only reagent approved by the U.S. Food and Drug Administration (FDA) for clinical applications and has been widely used in medical imaging and diagnosis.[29] ICG can be activated by 808 nm light to produce ROS, especially $^1O_2$,[30] showing a significant PDT effect. In addition, ICG is a negatively charged photosensitizer. Each ICG molecule contains one cationic pyrrole group and two anionic sulfonic acid groups, with a total charge of minus one at neutral pH, which can combine with positively charged nanoparticles through electrostatic interactions.[31,32] However, PS continuously consumes oxygen, which weakens the therapeutic effectiveness of PDT. To address this problem, some reports have used catalysts (iron and manganese) or nano-enzymes to catalyze the endogenous H_2O_2 to produce oxygen *in situ*,[33,34] but the concentration of H_2O_2 in cells is limited. Thus, it is necessary to develop an intelligent delivery system with adequate oxygen supply to generate a better therapeutic effect of PDT. Perfluorohexane (PFH), a liquid perfluorocarbon, is used as a blood substitute due to its good biocompatibility, high oxygen affinity, and large oxygen storage capacity.[35,36] In addition, PFH with a boiling point of about 57 °C is prone to undergo a phase transition from liquid to gas, achieving a fast release of oxygen.[37,38] Moreover, $^1O_2$ in PFH is reported to be more stable than $^1O_2$ in the cellular environment or water, resulting in a long-lasting PDT effect.[39] Hence, constructing a photosensitizer carrying oxygen-saturated PFH can improve the therapeutic effect of PDT. In addition, oxygen is required for various wound healing processes, including epithelial cells, angiogenesis, and collagen deposition, which are necessary to restore tissue function and integrity. Adequate wound tissue oxygenation can trigger a healing response and help to influence the outcome of other treatments.[40]

Herein, we report the development of a mesoporous carbon nanoplatform (CIL@ICG/PFH@O_2) with surface modification by cationic ionic liquids (ILs) that attract anionic ICG to provide a NIR-triggered O_2 diffusion enhanced PTT/PDT synergistic antimicrobial therapy. The mesoporous nanoplatform can effectively load oxygen saturated liquid PFH, acting as an oxygen carrier, and electrostatically load ICG through anion exchange with the surface-grafted ILs. With single-wavelength (808 nm) NIR laser irradiation, the local temperature of the carbon nanoparticles increased rapidly due to the wide wavelength absorption range and high photothermal conversion efficiency, which may promote the gasification of PFH and significantly accelerate the release of O_2 from CIL@ICG/PFH@O_2, thus rapidly activating and enhancing the PDT effect of ICG. After 5 min of 808 nm light treatment, CIL@ICG/PFH@O_2 demonstrated effective bactericidal activities against methicillin-resistant *Staphylococcus aureus* (MRSA) and kanamycin-

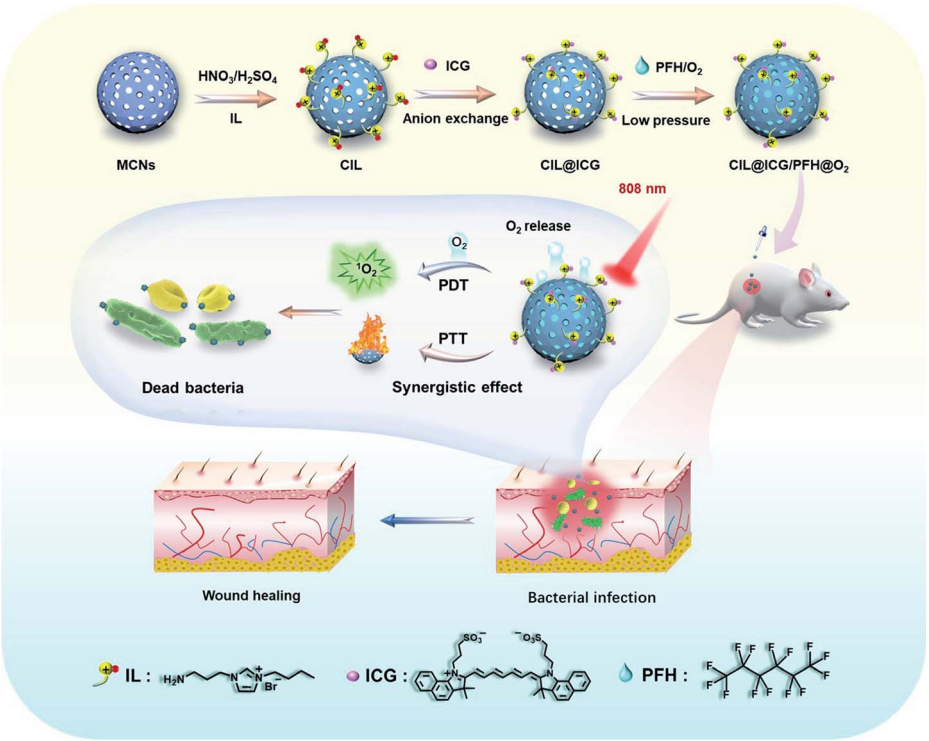

Scheme 1 Schematic illustration of the synthesis of CIL@ICG/PFH@O_2 nanoparticles and their corresponding synergistic antibacterial mechanism under single wavelength (808 nm) NIR irradiation. CIL@ICG/PFH@O_2 showed bactericidal activities against drug-resistant bacteria both *in vitro* and *in vivo*.

resistant *Escherichia coli* (BL21), due to the combination of PTT and enhanced PDT effects. More importantly, CIL@ICG/PFH@O_2 has good biocompatibility and has been shown to effectively inhibit MRSA-induced wound infection and promote wound healing in mouse animal models.

Results and discussion

Preparation and characterization of CIL@ICG

To effectively inhibit and eliminate drug-resistant bacterial infections, antibacterial mesoporous carbon nanoparticles (MCNs) with PTT and enhanced PDT activities were synthesized as shown in Scheme 1. MCNs grafted with ILs can effectively load liquid PFH as an oxygen carrier as well as electrostatically combine the anionic photosensitizer ICG *via* anion exchange with the surface grafted ILs, which is expected to kill bacteria *in vitro* and *in vivo* through enhanced PDT and PTT effects under 808 nm laser irradiation. MCNs were first prepared according to a low-concentration hydrothermal route,[41] and the morphology was observed from the SEM and TEM images. As shown in Fig. 1a, the resulting MCNs were uniformly spherical with a diameter of approximately 100 nm, and arranged mesoporous structures (about 4 nm) could be seen. After MCNs were oxidized (denoted as OMCNs) and further grafted with 3-butyl-1-aminopropylimidazolium bromide (named CIL), the spherical structures did not change significantly, and most of the mesoporous structures were retained (Fig. 1b and c). While the average hydrodynamic diameter of MCNs, OMCNs and CIL increased gradually, they were found to be about 99, 116, and 151 nm in diameter, respectively (Fig. 1d), which is comparable to the particle size observed by SEM. The increased size may be induced by the hydrophilic carboxyl groups produced by oxidation and grafted hydrophilic ILs.

Nitrogen adsorption–desorption isotherm measurements at 77 K revealed that MCNs had a surface area of 687 $m^2\ g^{-1}$, showing a relatively high specific surface area. Besides, the pore-size distribution calculated by nonlocal density functional theory (NLDFT) showed that the average pore size distribution was centered at 3.5 nm (Fig. S1a†). After oxidation and grafting of ILs, the surface area and pore size distribution were decreased to 508 $m^2\ g^{-1}$ and 3.2 nm (Fig. S1b†), and 386 $m^2\ g^{-1}$ and 2.7 nm (Fig. 1e), respectively, indicating that the oxidation process and the grafted ILs had a certain influence on the pore size of MCNs. FTIR spectroscopy was used to study the structural information of OMCNs, CIL, and CIL@ICG. As shown in Fig. S2,† OMCNs showed a strong absorption peak at 1721 cm^{-1} (C=O) due to the presence of the carboxyl group. After the grafting of ILs, the peak intensity of the amide group increased (1662 cm^{-1}), and the characteristic peak of the imidazole ring (1412 cm^{-1}) was observed, indicating that the ILs were grafted

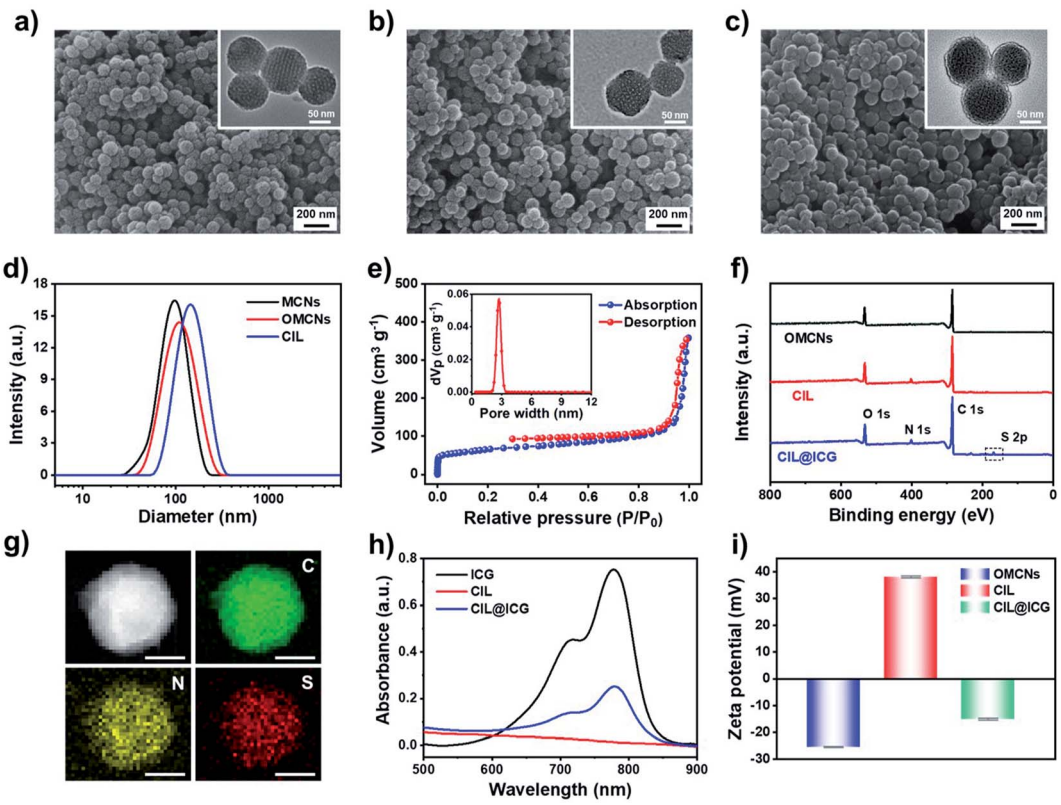

Fig. 1 SEM images of (a) MCNs, (b) OMCNs and (c) CIL; the inset displays the corresponding TEM images. (d) The size distribution of MCNs, OMCNs and CIL. (e) N_2 adsorption–desorption isotherms at 77 K and pore size distribution (inset) curves of CIL@ICG. (f) XPS spectra of OMCNs, CIL and CIL@ICG. (g) High-angle annular dark-field scanning TEM (HAADF-STEM) image and corresponding elemental (C, N, and S) mappings of CIL@ICG. (h) UV-vis-NIR spectra of ICG, CIL and CIL@ICG. (i) Zeta potential of OMCNs, CIL and CIL@ICG.

onto the OMCNs successfully. The photosensitizer ICG was loaded onto the CIL by anion exchange to form CIL@ICG, which simplified the procedure while also making ICG more stable and difficult to dissolve. A corresponding characteristic absorption peak of ICG at 1425 cm^{-1} appeared in the FT-IR spectrum of CIL@ICG (Fig. S2†), suggesting the introduction of ICG anions. The X-ray photoelectron spectroscopy (XPS) image in Fig. 1f shows that CIL yielded three major peaks centered at 285 (C 1s), 400 (N 1s), and 532 (O 1s) eV, among which the N orbital peak was mainly attributed to the grafted ILs on OMCNs surfaces, while OMCNs showed only two peaks at 285 (C 1s) and 532 (O 1s) eV. However, CIL@ICG exhibited an additional absorption peak at 168 eV, which corresponded to S 2p of ICG (Fig. S3†). The appearance of the S signal further illustrated that ICG was successfully introduced onto CIL. In addition, the element mapping measured by scanning transmission electron microscopy (STEM) displayed that the red S signals were uniformly distributed on the nanoparticles (Fig. 1g), revealing the presence of sulfur-containing ICG in CIL. The absorption peaks of ICG at 700–800 nm appeared in CIL@ICG and not in CIL, which also demonstrated the successful introduction of ICG (Fig. 1h). Furthermore, the zeta potentials of OMCNs, CIL and CIL@ICG confirmed surface modification (Fig. 1i). The OMCNs showed a negative zeta potential of -25 ± 0.2 mV, while the zeta potential turned positive to 38 ± 0.4 mV after being grafted with ILs, which was attributed to the positive charge of ILs. However, after anion exchange with ICG, the zeta potential of the nanoparticle dropped to negative (-15 ± 0.3 mV) due to the negatively charged ICG in the grafted ILs.

The amount of ICG present in CIL@ICG was determined to be 7.56 μg per mg, evaluated from the UV-vis absorption results. The stability of CIL@ICG was further studied by monitoring the release of ICG from the UV-vis spectrum. Fig. S4† shows that the absorption peak increased with prolonged time, indicating that ICG could be released from CIL@ICG in PBS. The maximum release amount was reached after 50 min, and then the absorption peak decreased due to the instability of the released free ICG in aqueous solution. The photostability of ICG limits its application as a photosensitizer. Accordingly, the photostability of CIL@ICG/PFH@O_2 nanoparticles was studied. The absorption spectra of the free ICG solution and CIL@ICG/PFH@O_2 suspension under 808 nm NIR irradiation at different times were recorded. As shown in Fig. S5,† the absorption peak of the ICG solution decreased significantly after 10 min irradiation. However, the absorption peak of the CIL@ICG/PFH@O_2 suspension continuously increased within 8 min irradiation, which may be due to the sustained release of ICG caused by the photothermal effect. Afterwards, the absorption decreased slightly with prolonged irradiation time. These results indicate that the photostability of ICG in CIL@ICG/PFH@O_2 is higher than that of free ICG.

To determine the optimal conditions for low-temperature PTT, different concentrations (31.3–500.0 μg mL^{-1}) of CIL@ICG nanoparticles were exposed to 808 nm NIR irradiation. As shown in Fig. 2a, the temperature of CIL@ICG aqueous solutions increased gradually with irradiation time, indicating an obvious concentration-dependent temperature increase under NIR laser irradiation. Furthermore, a power density-dependent photothermal effect was also observed for CIL@ICG (Fig. 2b), which showed that the power of NIR laser irradiation had a positive correlation with the thermal effect of CIL@ICG. The infrared images were consistent with these results (Fig. 2c). ICG

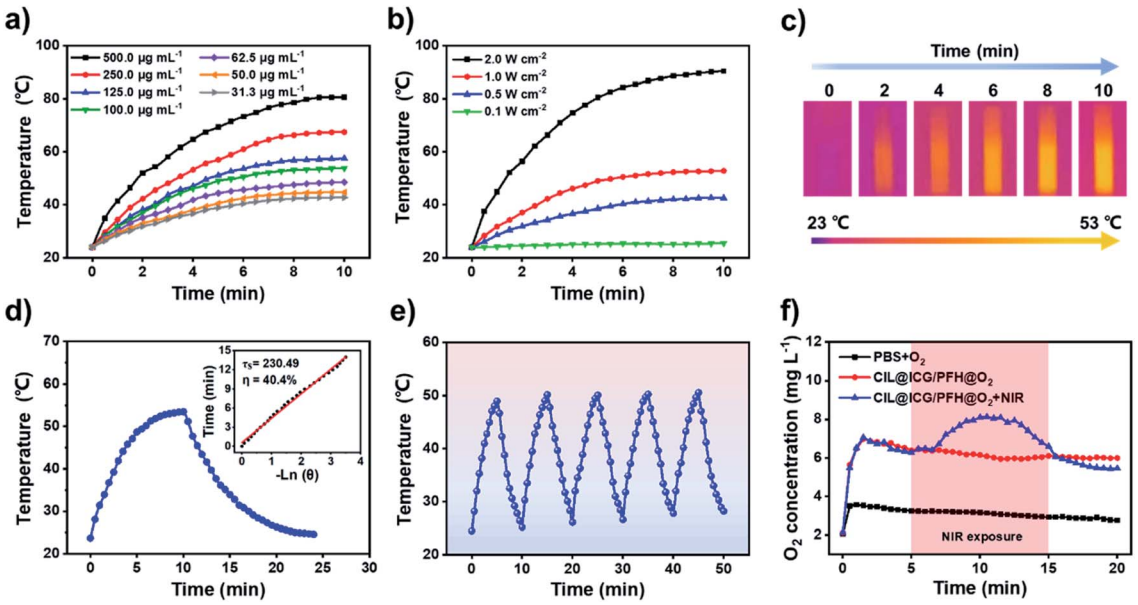

Fig. 2 (a) Time–temperature curves of the CIL@ICG solution with various concentrations under NIR laser irradiation (808 nm, 1 W cm^{-2}). (b) Time–temperature curves of the CIL@ICG solution (100 μg mL^{-1}) under different power density irradiations. (c) IR thermal images of the CIL@ICG solution with different times of laser irradiation. (d) Photothermal conversion efficiency and (e) photostability of CIL@ICG. (f) O_2 concentration changes of oxygen saturated PBS and the CIL@ICG/PFH@O_2 deoxygenated water suspension with and without NIR laser irradiation.

can also exert a photothermal effect, and the effect of ICG in the photothermal properties of CIL@ICG was further studied. The results in Fig. S6† suggest that the photothermal effect of CIL@ICG was mainly generated from CIL, while the contribution of ICG is limited. The photothermal conversion efficiency of CIL@ICG was further evaluated. As shown in Fig. 2d, the linear regression curve of CIL@ICG was obtained from the cooling curves according to a previous report.[42] The time constant for heat transfer (τ) was calculated to be 230.49 s, and the photothermal conversion efficiency (η) was 40.4%, indicating that CIL@ICG possessed relatively high photothermal conversion efficiency. Moreover, the CIL@ICG nanoparticles showed good photothermal stability, and a further temperature increase was not noticeable after five heating and cooling cycles (Fig. 2e).

PFH can dissolve oxygen gas effectively due to the strong van der Waals interactions between PFH and oxygen molecules.[37,43,44] Thus, CIL@ICG with a large specific surface area and a porous structure can serve as a good oxygen carrier to deliver oxygen after loading with PFH. As illustrated in Fig. S7,† small gas bubbles can be observed in CIL@ICG/PFH and CIL@ICG/PFH@O_2 dispersions under NIR irradiation, while no gas bubbles appeared in CIL@ICG dispersions. These gas bubbles are derived from the phase transition of PFH from liquid to gas and the released dissolved O_2 from PFH, indicating that PFH and O_2 were effectively loaded in the nanoparticles. The oxygen-carrying and release capabilities of CIL@ICG/PFH@O_2 were evaluated by detecting the concentration of dissolved oxygen in an aqueous solution with a real-time oxygen meter. Fig. 2f shows that the oxygen concentration increased significantly after adding CIL@ICG/PFH@O_2 and reached a maximum value of 7.0 mg L^{-1} at 1.5 min, which is much higher than that of the oxygen saturated PBS solution (3.6 mg L^{-1}). Thereafter, the CIL@ICG/PFH@O_2 suspension showed a much slower decrease in oxygen concentration and a higher final oxygen concentration compared to the oxygen saturated PBS solution within 20 min, suggesting that CIL@ICG/PFH@O_2 has good oxygen loading abilities and can ensure a gradual release of oxygen into the surrounding environment. In addition, the oxygen release activities of CIL@ICG/PFH@O_2 under 808 nm laser irradiation were further evaluated to study the effect of the photothermal effect on oxygen release. When exposed to the laser irradiation, the released oxygen concentration sharply increased and reached a maximum of 8.13 mg L^{-1}. This burst release may be due to an increase in temperature caused by the NIR-induced photothermal effect, which accelerates the vaporization of PFH and corresponding release of oxygen.

Antibacterial activity *in vitro*

Encouraged by the ROS production and photothermal conversion, the synthesized nanoparticles as nanoagents were evaluated for antibacterial phototherapy using a plate counting method against Gram-positive bacteria *S. aureus* and MRSA, and Gram-negative bacteria *E. coli* and BL21. The antibacterial activities of different concentrations of CIL@ICG/PFH@O_2 against MRSA and BL21 were first assessed with and without irradiation. As shown in Fig. 3a, b and S8,† the bacterial viability decreased as the concentration increased. When the concentration increased from 50 to 150 μg mL^{-1}, the bacterial viability of MRSA and BL21 decreased from 84.1% and 85.1% to 75.9% and 79.0%, respectively, in the dark. This sterilization effect is probably due to the strong electrostatic interaction between the imidazolium cations on the surface of CIL@ICG/PFH@O_2 and the negatively charged bacterial cell walls.[45,46] However, upon exposure to the NIR irradiation, the survival rates of MRSA and BL21 decreased sharply to less than 1% with the treatment of 100 μg mL^{-1} CIL@ICG/PFH@O_2, suggesting a promising sterilization effect. This good antibacterial effect may be induced by the synergism of electrostatic interactions with photodynamic and photothermal effects of CIL@ICG/PFH@O_2. These results suggest that the antibacterial activity of CIL@ICG/PFH@O_2 is positively correlated with the concentration and irradiation time. Therefore, 100 μg mL^{-1} CIL@ICG/PFH@O_2 and 808 nm laser irradiation (1.0 W cm^{-2}, 5 min) were applied as the experimental conditions to ensure that the concentration and power are suitable in the range of low hypothermia PTT.

To evaluate the PDT and PTT synergetic antibacterial activities of CIL@ICG/PFH@O_2, bacteria were treated with and without NIR (1 W cm^{-2}, 5 min) with 100 μg mL^{-1} of nanoparticles. As demonstrated in Fig. 3c–e and S9a,† the antibacterial activities of CIL and CIL@ICG were 71% and 90% for MRSA and 60.2% and 82.5% for BL21, respectively. The bactericidal activity of CIL@ICG/PFH@O_2 against MRSA and BL21 sharply increased to more than 99.9%, demonstrating a superior antibacterial activity. Such a significantly higher bactericidal efficiency was found to be associated with the photothermal and enhanced photodynamic properties as well as electrostatic interaction of CIL@ICG/PFH@O_2. Similar results were obtained against *S. aureus* and *E. coli* (Fig. S10†). These results demonstrate that CIL@ICG/PFH@O_2 possessed efficiently broad-spectrum antibacterial properties due to the synergistic effect of PTT and the oxygen supply enhanced PDT effect.

Live/dead staining was performed to verify the PTT/PDT bactericidal effects of the nanoparticles. The dead bacteria would emit red and green fluorescence after staining with PI and SYTO 9, whereas the viable bacteria can only be labeled with green fluorescence by STYO 9. Most MRSA and BL21 bacteria emitted apparent green fluorescence after treatment with various nanoparticles in the absence of NIR irradiation (Fig. 3f and S9b†), indicating that most bacteria remained viable. In comparison, the bacteria treated with CIL and CIL@ICG scattered obvious red fluorescence under NIR irradiation with a little green fluorescence, indicating that most of the bacteria were killed. In particular, more red fluorescent signals of dead bacteria were emitted after the treatment with CIL@ICG/PFH@O_2 and NIR irradiation, suggesting the efficient sterilization effect. These results were consistent with the antibacterial activity tested by the colony counting method, which demonstrated that CIL@ICG/PFH@O_2 might be a promising PDT/PTT therapeutic agent for future antibacterial therapy.

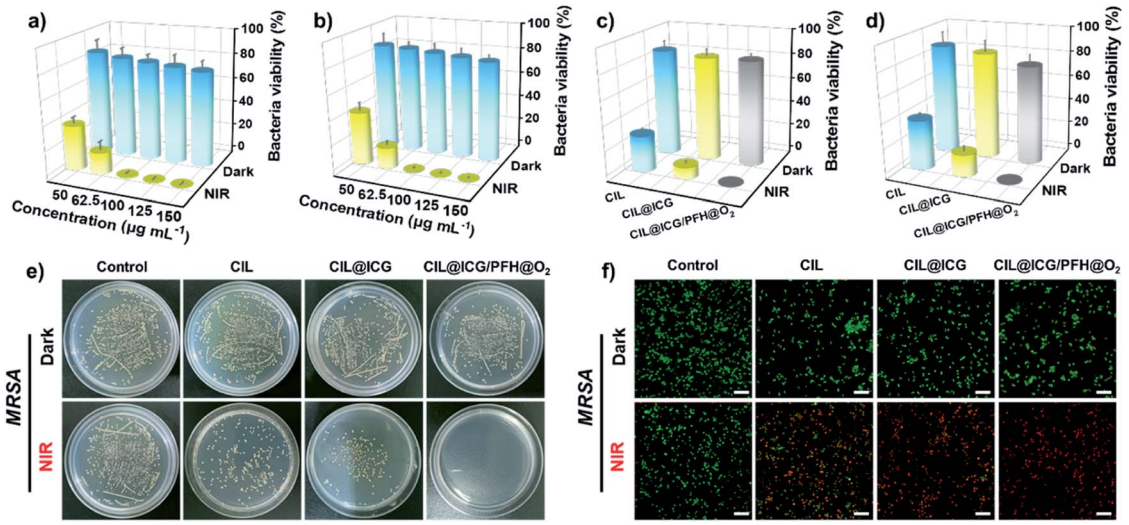

Fig. 3 The viabilities of (a) MRSA and (b) BL21 co-cultured with different concentrations of CIL@ICG/PFH@O_2 with/without 808 nm NIR irradiation. The viabilities of (c) MRSA and (d) BL21 with different treatments determined by the plate counting method. (e) Corresponding plate diffusion results and (f) live/dead fluorescence staining images of MRSA co-cultured with 100 μg mL^{-1} CIL, CIL@ICG and CIL@ICG/PFH@O_2 with and without 808 nm NIR irradiation. Red and green fluorescence represent dead and viable bacteria, respectively. Laser irradiation conditions: 1 W cm^{-2}; 5 min. Scale bar: 8 μm.

Antibacterial mechanism investigation

ROS play an important role in photodynamic cytotoxicity.[27,47] ICG could produce ROS effectively with laser irradiation in aqueous media. The introduction of the anionic photosensitizer ICG makes CIL@ICG produce ROS under NIR irradiation, which could oxidize and destroy the membranes of bacteria.[48] The ROS generation capacity of the synthesized nanoparticles was measured from the fluorescence spectra using DCFH-DA as a ROS probe. The fluorescence spectra in Fig. 4a show that there was no absorption in CIL at 520 nm regardless of NIR irradiation, indicating that CIL cannot produce ROS. However, a strong absorption peak at 520 nm appeared in CIL@ICG under NIR irradiation; the intensity was similar to that of CIL@ICG/PFH, suggesting a significant production of ROS. As for oxygen-loading CIL@ICG/PFH@O_2, the absorption peak significantly increased, which demonstrated that the loading of oxygen significantly enhanced the production of phototoxic ROS.[49] The results of CIL@ICG, CIL@ICG/PFH and CIL@ICG/PFH@O_2 without NIR exposure further clarified the necessity of NIR and oxygen for the generation of ROS. ESR spectroscopy is further conducted to identify the species of ROS.[50,51] Fig. S11† shows that no signal peak appeared in ICG without irradiation, whereas ICG induced three peaks with a relative intensity ratio of 1 : 1 : 1 after NIR irradiation, which was the representative TEMP-$^1O_2$ signal. Similarly, no signal peaks were observed in CIL@ICG without irradiation, while the TEMP-$^1O_2$ signal was generated after being exposed to NIR irradiation (Fig. 4b). Additionally, the loaded PFH in CIL@ICG did not affect the generation of $^1O_2$. However, the intensity of the $^1O_2$ signal in CIL@ICG/PFH@O_2 increased significantly, indicating that the loading of O_2 markedly enhanced the generation of $^1O_2$.

ROS can cause oxidative bacterial cell membrane and wall damage and diffuse into cells to further destroy the bacteria. Intracellular ROS of MRSA and BL21 were evaluated from the fluorescence spectra with DCFH-DA as a probe (Fig. 4c and d). The fluorescence intensity of bacteria treated with CIL, CIL@ICG and CIL@ICG/PFH@O_2 was extremely low and almost non-existent in the dark. Once exposed to NIR irradiation, there was no significant change in the fluorescence intensity of CIL, while the fluorescence intensity of CIL@ICG and CIL@ICG/PFH@O_2 was greatly enhanced, indicating a higher ROS level in bacterial cells. Notably, CIL@ICG/PFH@O_2 produced more ROS than CIL@ICG, indicating that oxygen loading could significantly increase the generation of ROS, leading to higher intracellular ROS levels. These relatively high ROS levels were essential for the synthesized carbon nanomaterials to exhibit effective bactericidal effects. Furthermore, O_2 levels in bacterial cells were also studied using $[Ru(dpp)_3]Cl_2$ as an oxygen probe to demonstrate the intracellular oxygen supply capacity of CIL@ICG/PFH@O_2. As shown in Fig. 4e, the fluorescence signals of the control, CIL and CIL@ICG groups were basically similar regardless of NIR irradiation, suggesting that the intracellular oxygen levels in bacteria are limited. However, noticeably weakened fluorescence was observed in CIL@ICG/PFH@O_2 treated bacteria, which indicated that CIL@ICG/PFH@O_2 could effectively supply oxygen to bacteria. After irradiation with NIR, fluorescence signals became invisible in CIL@ICG/PFH@O_2 treated bacteria, suggesting that the laser irradiation exerts an auxiliary effect on oxygen supplementation.

Both the existing ILs and produced ROS would destroy the bacterial membranes. Fluorescence analysis could prove the membrane disruption antibacterial mechanism.[52] cFDA-SE is a permeable dye for bacterial cell walls and membranes, which would emit fluorescence at 518 nm after esterase hydrolysis. As illustrated in Fig. 4f and g, the emission peak at 518 nm was very weak after being treated with different nanoparticles without

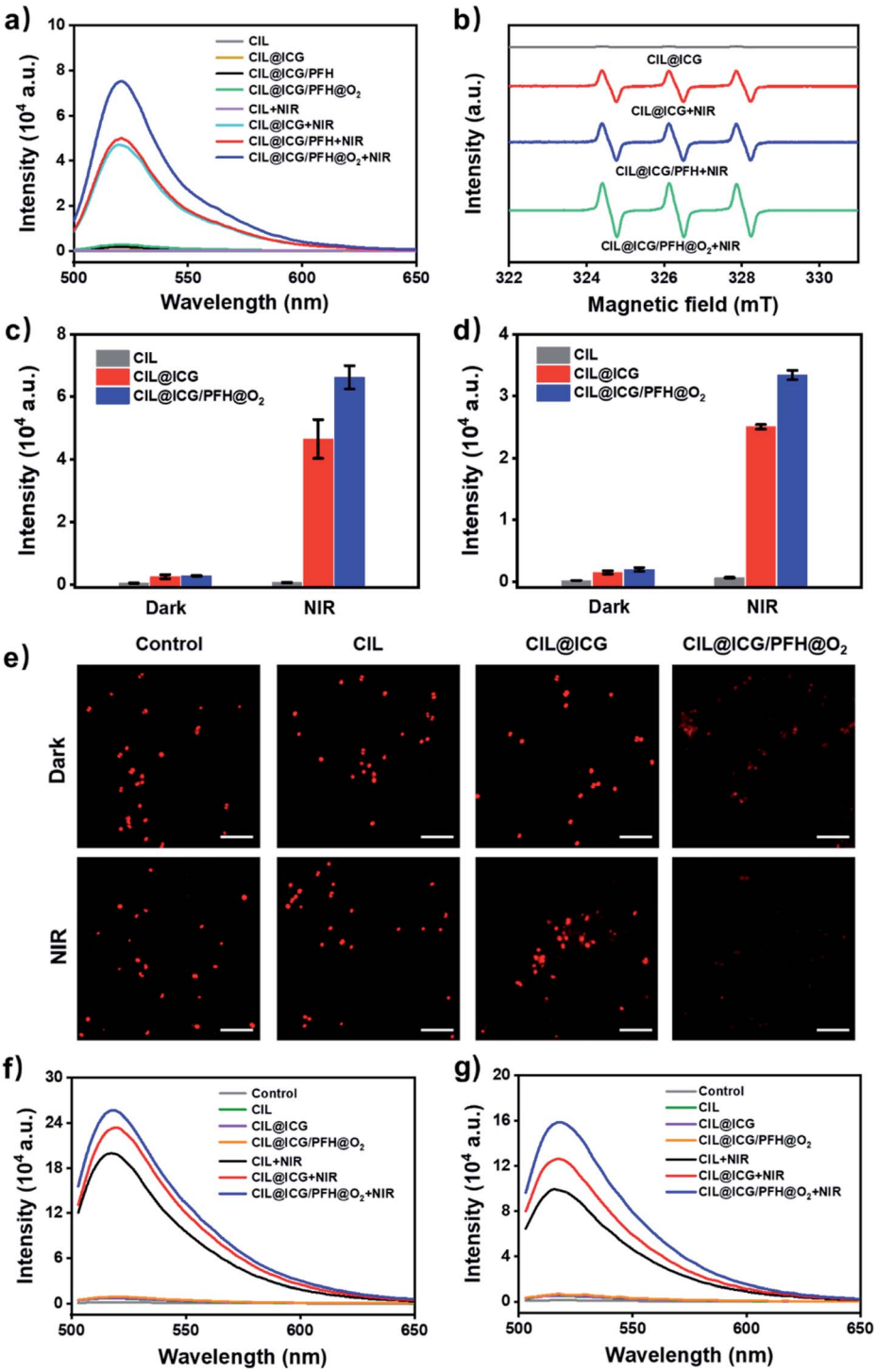

Fig. 4 (a) Fluorescence spectra of DCFH-DA in the presence of CIL, CIL@ICG, CIL@ICG/PFH and CIL@ICG/PFH@O_2, with and without 808 nm NIR irradiation. (b) ESR spectra of the synthesized nanoparticles to detect $^1O_2$ with/without irradiating under NIR for 5 min. Fluorescence intensity of ROS in (c) MRSA and (d) BL21 with different treatments using DCFH-DA as a probe. (e) Fluorescence images of MRSA bacterial cells stained with $[Ru(dpp)_3]Cl_2$ after different treatments. Scale bar: 8 μm. cFDA-SE leakage assay of (f) MRSA and (g) BL21 with different treatments detected from the fluorescence spectrum. Bacteria treated with PBS were used as the control group. Laser irradiation conditions: 1 W cm^{-2}; 5 min.

NIR irradiation, indicating only partial disruption to bacterial membranes by the ILs modified on the surface of nanoparticles. However, the fluorescence intensity of the bacteria treated with CIL increased significantly after 5 min of NIR irradiation, which may be due to the PTT-induced bacterial membrane destruction. In comparison, the emission peak intensity of CIL@ICG further increased due to the synergistic effect of PTT and PDT against the bacterial cells. Due to the oxygen-supplied enhanced

PDT effect, the emission peak of CIL@ICG/PFH@O_2 increased sharply. These findings indicated that the nanoparticles can efficiently kill bacteria through a membrane destruction mechanism.

SEM images show the morphological changes of bacteria treated with different nanoparticles (Fig. S12†), and MRSA and BL21 bacteria in the control groups showed a normal shape with a smooth surface and intact cell walls. After being treated with different nanoparticles in the dark, almost all MRSA and BL21 morphologies remained unchanged, with only a few bacterial membranes being damaged. However, once the bacteria were treated with nanoparticles and exposed to 1 W cm^{-2} NIR for 5 min, wrinkles and obvious damage were observed on the bacterial surface as indicated by red arrows, indicating the complete morphological destruction of the bacteria due to photothermal effects and ROS production. When bacteria were treated with CIL@ICG/PFH@O_2 under NIR irradiation, more of them collapsed and fused, apparently due to cytoplasm leakage. These results suggest that sufficient heat and high ROS levels caused the destruction of bacterial cell membranes and the leakage of the intracellular matrix, which ultimately leads to bacterial death.

Hemocompatibility and cytocompatibility

The biocompatibility of antibacterial agents is another key factor for the practical application *in vivo*. The hemolysis assay demonstrated that no obvious hemolytic effect was observed in the supernatant treated with PBS and different CIL@ICG/PFH@O_2 solutions (62.5–500.0 μg mL^{-1}) after being in contact with red blood cells for 3 h, while the supernatant treated with Triton X-100 was bright red (Fig. 5a). In addition, even if the concentration of CIL@ICG/PFH@O_2 is as high as 500.0 μg mL^{-1}, the hemolysis rate was only 3.12%, which was lower than the critical safe hemolytic ratio of 5%.[22] Furthermore, the cytotoxicity of the nanoparticles towards mammalian cells was assessed by MTT assay using HaCaT cells as a model. It was found that the cell viability of HaCaT cells in all experimental groups was over 90% with and without NIR irradiation (Fig. 5b). Compared with the groups in the dark, the survival rate of HaCaT cells with NIR irradiation was slightly lower, possibly because the heat and ROS generated after irradiation had a certain effect on the cells. Moreover, the relative survival rates of the three irradiated groups were 91.13%, 92.14%, and 94.58%, respectively, with an increasing trend, indicating that the introduction of biocompatible ICG and PFH in MCNs would not affect cell growth. These findings showed that the synthesized nanoparticles were nontoxic and well biocompatible with animal cells, which made them suitable for the treatment of bacterial infections *in vivo*.

In vivo treatment of MRSA-infected wounds with CIL@ICG/PFH@O_2

The synergistic antibacterial and wound healing therapeutic efficacies of the CIL@ICG/PFH@O_2 nanoparticles were further evaluated *in vivo* using a mouse model bearing drug-resistant bacteria-induced cutaneous wounds (Fig. 6a). The animal model of the bacterially infected wound was established by making an 8 mm cut on the back of each mouse followed by inoculation with the MRSA suspension (1×10^8 CFU mL^{-1}) for 30 min. The wound without the MRSA suspension was a negative control group. The photothermal efficacy of CIL@ICG/PFH@O_2 *in vivo* indicated that the temperature of the infected wound tissues increased from 26.1 °C to 50.0 °C after irradiation with NIR (808 nm, 1 W cm^{-2}) for 10 min, proving that CIL@ICG/PFH@O_2 exhibited an effective PTT effect *in vivo* (Fig. 6b and S13†). Simultaneously, no significant damage was observed in the heat-treated skin tissue. The representative images of MRSA-infected wounds on days 0, 2, 4, 8, and 12 are shown in Fig. 6c. A severe inflammatory response was observed in the PBS-treated wounds (positive control group) after 2 days, and due to the severe infection, the wounds still showed obvious erythema even after 12 days. Compared with the positive control group, the infected wounds in the CIL@ICG/PFH@O_2 group without NIR irradiation showed a reduced

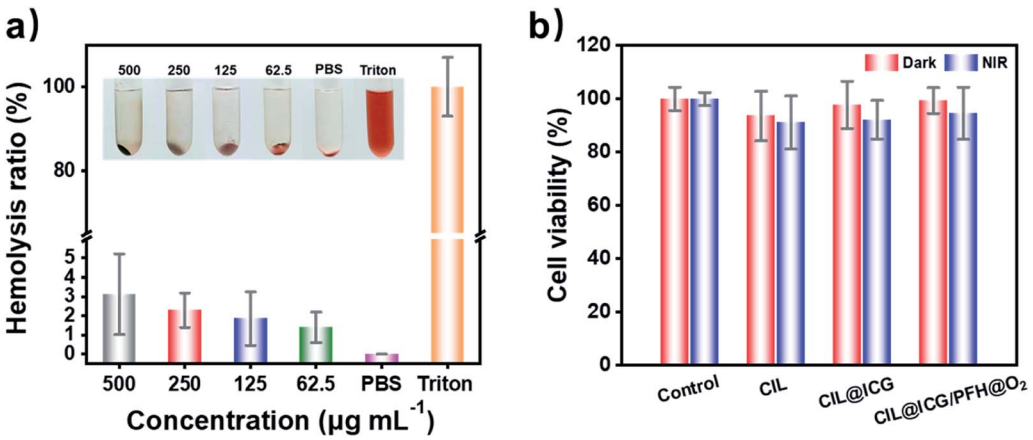

Fig. 5 (a) Hemolysis rate of CIL@ICG/PFH@O_2 after incubation with red blood cells at various concentrations (62.5–500.0 μg mL^{-1}) for 3 h. PBS and Triton X-100 solution were used as negative and positive controls, respectively. Inset: hemolysis photo after centrifugation. (b) Cell viability of HaCaT cells treated with CIL, CIL@ICG and CIL@ICG/PFH@O_2 for 0 and 5 min, under 808 nm NIR irradiation and cultured for 24 h. Laser irradiation conditions: 1 W cm^{-2}; 5 min.

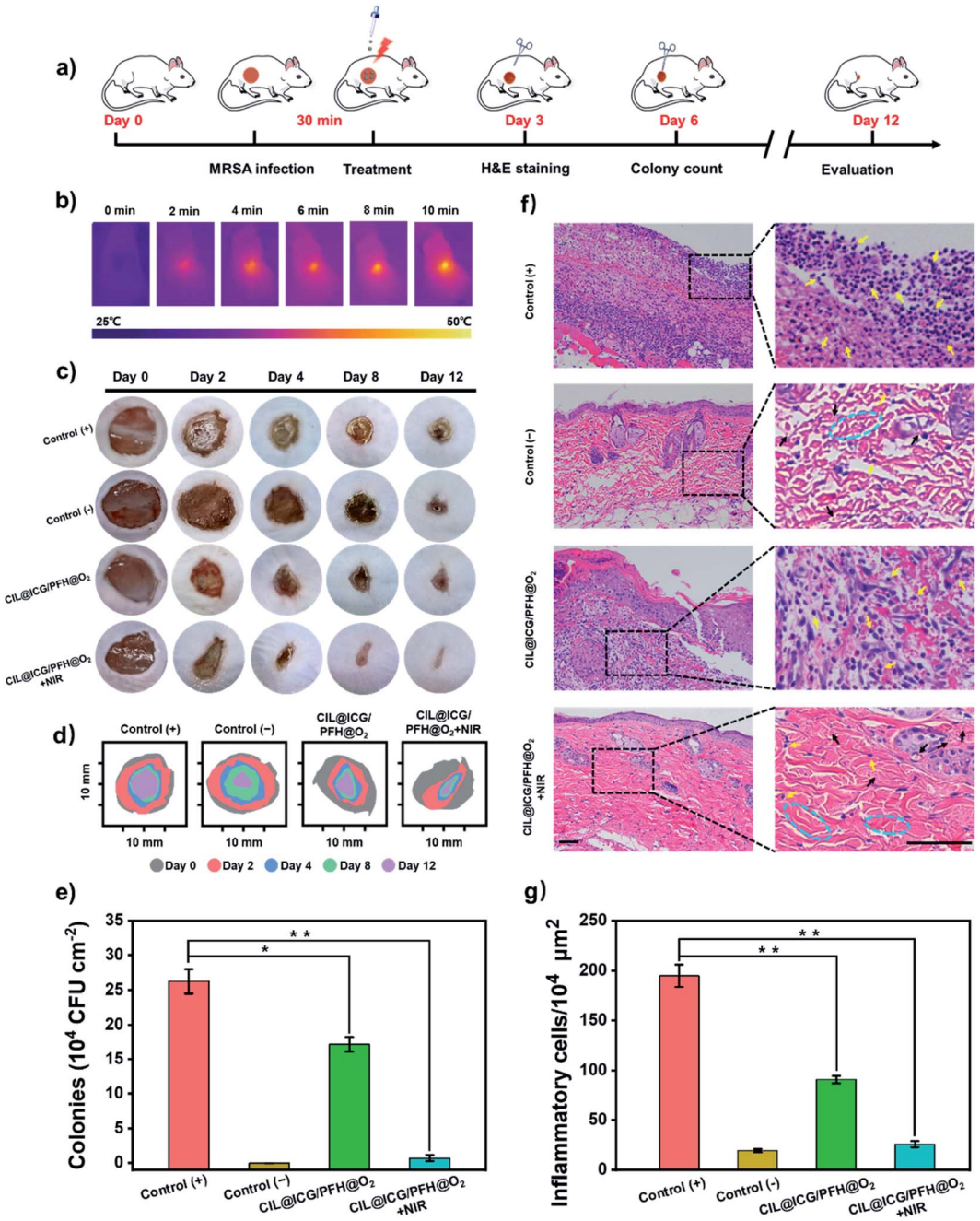

Fig. 6 (a) Schematic illustration of the evaluation of *in vivo* therapeutic efficacy of the CIL@ICG/PFH@O_2 nanoparticles. (b) Thermal images of a mouse treated with CIL@ICG/PFH@O_2 (100 μg mL^{-1}) at different times under NIR irradiation (808 nm, 1 W cm^{-2}). (c) Photographs of the mouse wounds from the four groups at different times during the therapeutic process. (d) The schematic diagram of the wound healing process. (e) Number of bacterial colonies isolated from wound tissue of mice in different treatment groups on day 6. (f) H&E staining of wound slices after different treatments on day 3. Yellow arrows: inflammatory cells, black arrows: blood vessels, and blue dotted cycles: collagen. (Scale bar: 50 μm). (g) The count of inflammatory cells per 10^4 square microns based on the corresponding pictures of H&E staining.

inflammatory response after 12 days, whereas the infected wounds in the CIL@ICG/PFH@O_2 + NIR group healed significantly after 12 days, even better than the negative control group. Moreover, the wound closure rates on day 12 were quantitatively assessed. The wound healing rates of the positive control group, negative control group, CIL@ICG/PFH@O_2 group, and CIL@ICG/PFH@O_2 + NIR group were 61.4%, 83.2%, 75.3%, and 90.9%, respectively (Fig. 6d), proving that CIL@ICG/PFH@O_2 nanoparticles could effectively treat the bacteria-infected wounds and promote wound healing by the synergistic effect of PTT and PDT under NIR irradiation. In addition, the skin tissue of the wound was cut off after treatment on day 6 to determine the residual bacteria within the lesions. The number of viable bacteria in wound tissue on day 6 was quantitatively studied by

the plate counting method to evaluate the antibacterial activity *in vivo*. As illustrated in Fig. 6e and S14,† the number of surviving bacteria in wound tissue treated with CIL@ICG/PFH@O_2 + NIR was 7.31×10^3 CFU cm^{-2}, which was much lower than those in the positive control group (2.63×10^5 CFU cm^{-2}) and CIL@ICG/PFH@O_2 group (1.71×10^5 CFU cm^{-2}). These results demonstrated good antibacterial properties of CIL@ICG/PFH@O_2 nanoparticles *in vivo* under the NIR irradiation.

The wound skin sections were stained with hematoxylin–eosin (H&E) for histological analysis on day 3 after treatment to evaluate the inflammatory effect and assess the wound curing process. As shown in Fig. 6f and g, a significant number of inflammatory cells were observed in the positive control group (194.67 per 10^4 μm^2), indicating severe infection in the wounds, while there were negligible inflammatory cells in the negative control group (19.42 per 10^4 μm^2). Compared with the positive control group, the number of inflammatory cells in the CIL@ICG/PFH@O_2 treated group reduced to 90.65 per 10^4 μm^2, and thick scar tissue was observed, indicating that there was still an obvious inflammatory response. New granulation tissues and newly formed epidermis were observed in the CIL@ICG/PFH@O_2 + NIR treated group. Moreover, only a few inflammatory cells (25.88 per 10^4 μm^2) appeared, and the tissue structure showed better regularity. Simultaneously, the appearance of small scar tissue with thickened epidermis, newborn collagen tissue and apparently visible neovascularization suggested an effective and potent wound healing effect of CIL@ICG/PFH@O_2 under NIR irradiation. The H&E staining results indicated that CIL@ICG/PFH@O_2 could effectively alleviate the inflammatory response and prevent bacterial infection *via* the PTT/PDT effect under NIR irradiation. In addition, the oxygen released from CIL@ICG/PFH@O_2 can help to accelerate wound healing by promoting collagen deposition, epithelial formation and blood vessel formation. Taken together, the CIL@ICG/PFH@O_2 nanoparticles could effectively prevent wound infection *via* synergistic PTT/PDT under NIR irradiation and further accelerate wound healing in the mouse model.

Conclusions

In this work, oxygen-loaded mesoporous carbon nanoparticles (CIL@ICG/PFH@O_2) were successfully prepared, as a single-wavelength activated PTT/PDT integrated therapeutic nanoplatform, with significantly enhanced O_2 diffusion and a promoted PTT/PDT effect. The prepared mesoporous carbon nanoparticles were modified with cationic ILs to introduce the anionic photosensitizer ICG through anion exchange while adsorbing onto negatively charged bacteria *via* electrostatic and hydrophobic interactions. In addition, the mesoporous structure of the carbon nanoparticles could load oxygen-soluble PFH at low pressure for use as an oxygen carrier. It was found that upon irradiation with a single-wavelength NIR laser (808 nm), CIL@ICG/PFH@O_2 concentrated the absorbed light energy into heat, accelerated the release of O_2, and rapidly activated and enhanced the PDT effect of ICG, inducing the combined treatment of PTT and enhanced PDT to sterilize drug-resistant bacteria BL21 and MRSA. Furthermore, CIL@ICG/PFH@O_2 demonstrated good biocompatibility, an effective antibacterial activity, reduced inflammation, and promoted wound healing in MRSA infected wounds *in vivo*. Therefore, the construction of CIL@ICG/PFH@O_2 nanoparticles, as a multifunctional nanoplatform to combine oxygen-enhanced and single-wavelength laser-controlled PTT/PDT co-therapeutic strategies, may provide a forward-looking strategy to confront drug-resistant bacterial infections.

Experimental

Materials

Phenol, formalin aqueous solution, sodium hydroxide (NaOH), the triblock copolymer Pluronic F127, indocyanine green (ICG), *N*-(3-aminopropyl)-imidazole, Boc anhydride, 1-bromobutane, *N*-hydroxysuccinimide (NHS), 1-[3-(dimethylamino)propyl]-3-ethylcarbodiimide hydrochloride (EDC), 2-(4-morpholino)ethanesulfonic acid (MES), sulfuric acid (H_2SO_4), nitric acid (HNO_3), ethanol, perfluorohexane (PFH), a polyethylene terephthalate (PET) membrane, 2,7-dichlorofluroescin diacetate (DCFH-DA), carboxyfluorescein diacetate-succinimidyl ester (cFDA-SE), tris(4,7-diphenyl-1,10-phenanthroline)ruthenium(II) dichloride $[Ru(dpp)_3]Cl_2$, propidium iodide (PI), SYTO 9, 2,2,6,6-tetramethylpiperidine (TEMP) and phosphate buffered saline (PBS, pH = 7.4) were purchased from Sigma-Aldrich Co., Ltd. All reagents were analytical grade and used as received without further purification. The Luria–Bertani broth medium (LB) and Dulbecco's modified Eagle medium (DMEM) are purchased from Biosharp. Deionized water was purified with a Milli-Q water system. *Staphylococcus aureus* (*S. aureus*, ATCC 6538), *Escherichia coli* (*E. coli*, 8099), and methicillin-resistant *S. aureus* (MRSA, ATCC 33591) strains obtained from Dr Sheng wen Shao (Huzhou University, School of Medicine, China), and Kanamycin-resistant *E. coli* (BL21, DE3) containing the plasmid pET28a obtained from Dr Yanran Chen (Shanghai Institute of Biochemistry and Cell Biology, Chinese Academy of Sciences, China) were used as model microorganisms.

Characterization

^{1}HNMR spectra of the synthesized substances were recorded on a Varian 400 MHz spectrometer with DMSO-d_6 as a deuterated solvent. The FT-IR spectra of the carbon nanoparticles were recorded on an IRTracer-100 in the range of 600–4000 cm^{-1}. UV-vis absorption spectra were recorded at room temperature using a UV-1900 ultraviolet spectrophotometer. XPS measurement was carried out using an XPS-7000 spectrometer (Rigaku, Japan) with a Mg Kα X-ray source. Brunauer–Emmett–Teller (BET) surface areas were measured at 77 K with a Micromeritics ASAP 2020 instrument for N_2 adsorption/desorption analysis. The nonlocal density functional theory (NLDFT) model was used to evaluate the pore-size distribution plots. Transmission electron microscopy (TEM) and scanning electron microscopy (SEM) images were recorded on a Tecnai G20 and a Hitachi S-4700, respectively, to observe the morphology of the nanoparticles and the micro-morphology of the bacteria. High-angle annular

dark-field scanning TEM (Tecnai G2 F20) was used to obtain element mapping. Electron spin resonance (ESR) spectroscopy (JES-X320, Japan) was carried out to confirm the generation of ROS under near-infrared (NIR) light at room temperature. The zeta-potential and hydrodynamic diameters of carbon nanoparticles were measured using a Zetasizer instrument (Nano ZS, Malvern Instruments Ltd). Bacterial fluorescence images were taken with a fluorescence microscope (Leica DM2500) with a 100× objective. The optical density (OD) values of bacterial suspensions were determined with a microplate analyzer (Thermo Fisher Scientific Multiskan GO). The light irradiation source was a near-infrared lamp with a wavelength of 808 nm.

Synthesis of 3-butyl-1-aminopropylimidazolium bromide

3-Butyl-1-aminopropylimidazolium bromide ([BAIm][Br]) was synthesized according to previous reports.[53] Typically, the amine group of *N*-(3-aminopropyl)-imidazole was first protected by Boc anhydride. The protected *N*-(3-aminopropyl)-imidazole and 1-bromoheptane were stirred in acetone solution at 60 °C for 72 h for the alkylation reaction. Afterwards, the product was reacted with HBr in methanol at 80 °C for 3 h to remove the Boc group, and the precipitate was filtered and washed with methanol to obtain [BAIm][Br]. ^{1}H NMR (400 MHz, DMSO-d_6, δ): 8.64 (s, J = 1.6 Hz, 1H), 7.89 (s, J = 2.4 Hz, 1H), 7.31 (dd, J = 15.3, 8.4 Hz, 1H), 4.75 (t, J = 5.6 Hz, 2H), 4.12 (t, J = 7.3 Hz, 2H), 2.71–3.06 (m, 4H), 2.15 (m, 2H), 1.53 (s, 2H), 1.40 (m, 2H), and 0.77 (t, J = 5.9 Hz, 3H).

Preparation of mesoporous carbon nanoparticles (MCNs)

Briefly, phenol (0.60 g), formalin aqueous solution (2.10 mL, 37 wt%) and NaOH aqueous solution (15.00 mL, 0.10 M) were mixed and reacted at 70 °C for 0.5 h to obtain a low molecular weight phenolic prepolymer. Afterwards, 0.96 g triblock copolymer Pluronic F127 dissolved in 15.00 mL H_2O was added to the above solution and stirred at 340 ± 40 rpm at 66 °C for 2 h. Then, 50.00 mL H_2O was added and stirred at 70 °C until the solution changed from transparent to pink, forming flocculent precipitates, and the reaction was stopped. This process would take 18 to 24 h approximately. After the mixture was cooled to room temperature, 56.00 mL H_2O was added to 17.70 mL of the mixed solution and transferred into an autoclave to heat at 130 °C for 24 h. The products were collected by centrifugation, washed with water several times and dried under vacuum. The carbonization was carried out in a N_2 atmosphere at a rate of 5 °C min^{-1} at 700 °C for 3 h to obtain mesoporous carbon nanoparticles.[41]

Oxidization of MCNs (OMCNs)

The resulting MCNs were suspended in a mixture of sulfuric acid (98%) and nitric acid (70%) with a ratio of 3 : 1 (v_1/v_2), and the suspension was treated with ultrasound at 35–40 °C for 1 h. The oxidized MCNs were collected by using a high-speed centrifuge and washed with water until the pH was neutral. Finally, the obtained OMCNs were freeze-dried overnight.

Preparation of IL grafted OMCNs (CIL)

ILs [BAIm][Br] were grafted to OMCNs by imitation of diimide activation, and the synthesis process was slightly modified from previous studies.[54] Briefly, 0.1 g OMCNs was dispersed in MES buffer (pH 6.0), then activated by the addition of EDC (240 mg) and NHS (173 mg) and continuously stirred at 25 °C. After 1 h, [BAIm][Br] (328 mg) dissolved in MES (5 mL) was dropped into the activated MCNs suspension and stirred at room temperature for 24 h. Finally, the CIL was collected by centrifugation and washed several times with water to remove any excess raw material. The CIL was obtained after drying under a high vacuum.

Synthesis of CIL@ICG

CIL@ICG was prepared by anion exchange. Typically, the positively charged CIL nanoparticles were mixed with the anionic photosensitizer ICG solution (0.2 mg mL^{-1}). The mixture was stirred in the dark for 6 h at room temperature. The products were centrifuged and washed with 20% methanol 3 times to remove the unreacted ICG. The obtained CIL@ICG was dried in a high vacuum overnight.

PFH loading, oxygen saturation and measurement of O_2 release

PFH was loaded into CIL@ICG nanoparticles before being saturated with O_2.[35,55] After freeze-drying, CIL@ICG (5 mg) was transferred into a sealed bottle (50 mL). After vacuuming, 50 μL of PFH was injected into the bottle and sonicated at 0 °C for 5 min. Afterwards, 1 mL of PBS was injected into the bottle and sonicated for another 10 min. Then, 1 mL PFH loaded CIL@ICG was dispersed in PBS in a 50 mL tube, which was stored in a sterile oxygen chamber (O_2 flow = 5 L min^{-1}) for 15 min to saturate oxygen. Finally, the oxygen-saturated, PFH-loaded CIL@ICG (CIL@ICG/PFH@O_2) was obtained.

The released oxygen concentration of CIL@ICG/PFH@O_2 in aqueous solutions was measured using a portable dissolved oxygen meter (Rex, JPB-608A, China). To measure O_2 release, 15 mL of deoxygenated water was added to a 50 mL flask filled with nitrogen. The electrode probe of the dissolved oxygen meter was inserted into the flask to measure the oxygen concentration of the solution in a timely manner. After injecting 5 mL oxygen-saturated CIL@ICG/PFH@O_2 (5 mg mL^{-1}) or PBS into the above flask, the oxygen concentration was evaluated for 20 min with a frequency of every 30 s. For the measurement of O_2 release triggered by the NIR laser, the CIL@ICG/PFH@O_2 suspension was irradiated by using an 808 nm laser (1 W cm^{-2}) for 10 min.

Photothermal effect of the synthesized nanomaterials

To evaluate the photothermal properties of CIL@ICG, 300 μL of CIL@ICG suspension at various concentrations was irradiated with a NIR laser (808 nm, 1 W cm^{-2}) for 10 min, and the real-time temperature was recorded every 30 s. In addition, the photothermal properties of 100 μg mL^{-1} CIL and the equivalent ICG solution were evaluated by following the same steps described above. A similar method was applied to record the

photothermal effect of CIL@ICG with a concentration of 100 μg mL^{-1} at different power densities.

The temperature of the CIL@ICG aqueous dispersion was recorded during the processes of heating (irradiated for 10 min with an 808 nm laser) and natural cooling to evaluate the photothermal conversion efficiency according to the following formula:

$$\eta = \frac{hS\Delta T_{max} - Q_w}{I\left(1 - 10^{-A_{808}}\right)} \times 100\% \quad (1)$$

where h and S are the heat transfer coefficient and the surface area of the glass tube, respectively. ΔT_{max} is the temperature change value when the system is in equilibrium. Q_w is produced by the photothermal conversion of water. I is the laser power of the input system, and A_{808} is the absorbance of the material at 808 nm.

Extracellular and intracellular reactive oxygen species (ROS) detection

A mixture of nanoparticles (1.5 mL, 200 μg mL^{-1}) and an equal volume of PBS with NaOH pretreated with DCFH-DA was irradiated with and without an 808 nm laser (1 W cm^{-2}) for 5 min. The ROS-generating abilities of the nanoparticles were evaluated by recording the fluorescence spectra (excitation wavelength of 485 nm; emission wavelength of 520 nm). For intracellular ROS detection, 1.0 mL of bacterial suspension was mixed with 10 μM DCFH-DA and cultured at 37 °C for 20 min. The centrifuged bacteria were then washed and re-suspended in a sterile PBS solution. After that, the nanomaterials were added to the bacterial solution with the final concentration of 100 μg mL^{-1}, with and without 808 nm laser irradiation for 5 min. The fluorescence intensity of bacteria was recorded to directly reflect the intracellular ROS.

Electron spin resonance characterization

2,2,6,6-Tetramethylpiperidine (TEMP) was used as a spin-trap to verify the generation of $^1O_2$. The mixture of TEMP and nanoparticles (100 μL, 100 μg mL^{-1}) was irradiated with/without an 808 nm laser at a power density of 1 W cm^{-2} for 5 min. Then, the mixture solution was transferred to capillary tubes ($d = 0.5$ mm) and detected in the cavity of the electron spin resonance (ESR) spectrometer at room temperature.

Evaluation of intracellular O_2 generation

The fluorescence of $[Ru(dpp)_3]Cl_2$ would be quenched by O_2, which was studied to evaluate the intracellular O_2 level. The bacterial solution was mixed with 10 μL of $[Ru(dPP)_3]Cl_2$ (10 μg mL^{-1}) which was cultured at 37 °C for 12 h. The centrifuged bacteria were then washed and re-suspended in a sterile PBS solution. Afterwards, the nanomaterials with the final concentration of 100 μg mL^{-1} were added to the bacterial solution. After being cocultured for 2 h, the bacteria were irradiated with and without 808 nm NIR and characterized by using a fluorescence microscope.

In vitro antibacterial assay

To evaluate the antibacterial activities of CIL@ICG/PFH@O_2, *E. coli*, and *S. aureus*, drug-resistant strains of BL21 and MRSA were selected as model microbes. Before determining antibacterial activity, the bacteria ($OD_{600\ nm} = 0.1$) were diluted to a certain concentration. 100 μL of diluted bacterial suspensions were mixed with an equal volume of the CIL@ICG/PFH@O_2 solution in a 96-well plate to make up the final concentrations of CIL@ICG/PFH@O_2 to 50, 62.5, 100, 125, and 150 μg mL^{-1}, respectively. The mixture was treated with and without an 808 nm laser (1 W cm^{-2}) for 5 min and incubated at 37 °C for 3 h. Bacteria treated with PBS were used as the control group. 10 μL of the bacterial suspension was plated on LB agar to incubate at 37 °C. After 18 h, the bacterial colonies on the plate were counted and recorded. The antibacterial rate was calculated as follows:

$$\text{Antibacterial activities } (\%) = \frac{N_0 - N}{N_0} \times 100\% \quad (2)$$

where N_0 is the number of colonies in the control group, and N is the number of colonies treated with the sample with/without light. Each colony assay test was repeated three or more times.

Live/dead bacterial staining assay

Live/dead staining assay was used to determine the bacterial viability with MRSA and BL21 as model microorganisms. The dye mixture of SYTO 9 and PI was added to the bacteria suspensions with different treatments. After being incubated in the dark for 15 min, the bacteria were centrifuged and washed with PBS three times to remove the free dyes. The stained bacteria were imaged on a fluorescence microscope using an oil immersed 100× objective lens.

Bacterial morphological characterization

A mixture of the bacterial suspension and the synthesized nanoparticles was dropped on aseptic PET films, which were irradiated with/without an 808 nm laser for 5 min. Bacteria treated with PBS were used as the control group. After incubation for 3 h at 37 °C, the supernatant was removed, and 2.5% glutaraldehyde solution was added to fix the bacterial cells for 2 h in the dark. Subsequently, the bacteria were dehydrated with 10%, 30%, 50%, 70%, 90% and 100% ethanol solutions for 10 min, respectively, before being characterized by SEM with gold sputtering coating.

Esterase activity assay

Carboxyfluorescein diacetate-succinimidyl ester (cFDA-SE) is a permeable dye for bacterial cell walls and membranes, which would become fluorescent upon hydrolysis by esterase of bacteria. The esterase activity of live bacteria can be detected by inverting the fluorescence change of the dye, which is positively related to bacterial membrane destruction. The bacterial suspension with $OD_{600\ nm} = 0.1$ was centrifuged at 5000 rpm for 2 min, washed with sterile PBS twice, and resuspended again with PBS. Then, the cFDA-SE ethanol solution with a final

concentration of 50 μM was added to the bacterial resuspension, and the mixture was co-cultured at 37 °C for 20 min. After centrifuging and washing twice with PBS, the precipitate was resuspended in 1.0 mL of PBS and treated with the synthesized nanoparticles, which were irradiated with/without an 808 nm laser for 5 min. The bacterial mixture treated with PBS was used as the control group. The fluorescence spectra were used to measure fluorescence intensity at ex 488 nm/em 518 nm.

Hemolysis assay

3 mL of fresh blood was centrifuged at 1500 rpm for 15 min to separate red blood cells (RBCs) from serum. The supernatant was removed, and the remaining RBCs at the bottom were thoroughly rinsed with PBS until the supernatant was colourless. The RBCs were then resuspended in PBS to form a 2% (v_1/v_2) suspension. 100 μL of CIL@ICG/PFH@O_2 solutions in PBS with different concentrations (62.5–500.0 μg mL^{-1}) were added into 100 μL of the RBC suspension in PBS. RBCs treated with PBS and Triton X-100 were used as negative and positive controls, respectively. The obtained RBC suspension was cultured at 37 °C for 3 h and then centrifuged at 2000 rpm for 15 min. 100 μL of the supernatant was taken out to record the OD value at 545 nm. The calculation formula for the hemolysis ratio of red blood cells is as follows:

$$\text{Hemolysis ratio } (\%) = \frac{OD_s - OD_n}{OD_p - OD_n} \times 100\% \quad (3)$$

where OD_s, OD_n, and OD_p are the optical density values of the samples, the negative control, and the positive control, respectively. All hemolysis tests were repeated three times.

Cytotoxicity evaluation

The cytotoxicity of the nanoparticles was assessed against HaCaT cells by 3-(4,5-dimethylthiazole-2-yl)-2,5-diphenyltetrabromazole (MTT) assay. HaCaT cells were seeded with DMEM in a 96-well plate at a density of 3×10^4 cells per well and incubated for 24 h at 37 °C. After discarding the supernatant, the nanoparticles (100 μg mL^{-1}) were added into the 96-well plate and irradiated with/without an 808 nm laser (1 W cm^{-2}) for 5 min. After co-culturing at 37 °C for 24 h, a medium containing 10% MTT solution (5 mg mL^{-1} in PBS) was added into each well to incubate for 4 h. Afterwards, the supernatant was discarded, and 150 μL of DMSO was added to each well to dissolve the produced formazan crystals. The absorbance at 570 nm was measured by using a microplate reader to assess cell viability. The cells treated with PBS were used as the control group. The viability of HaCaT cells was calculated by using the following formula:

$$\text{Cell viability } (\%) = \frac{OD_s}{OD_c} \times 100\% \quad (4)$$

where OD_s and OD_c are the optical density values of the samples and control, respectively. All the measurements were repeated three times.

In vivo MRSA-infected wound healing assay

All animal experiments were conducted in accordance with the national animal research code and approved by the Ethics Committee of Soochow University. 24 healthy male ICR mice (6–8 weeks old) were used for *in vivo* tests, and were randomly divided into four groups: (I) positive control, (II) negative control, (III) CIL@ICG/PFH@O_2, and (IV) CIL@ICG/PFH@O_2 + NIR. After feeding for 5 days, the mice were anesthetized by intraperitoneal injection of 2% sodium pentobarbital, and two wounds about 8 mm in diameter were made on their shaved backs. Afterwards, 25 μL of MRSA suspension (10^8 CFU mL^{-1}) was added onto the wound surfaces, and 25 μL of sterile PBS solution was added into the negative control group. After 30 min, different treatments were performed. Wounds in the (I) group were dripped with 25 μL sterile PBS and covered with sterile gauze, and the (II) group wounds were directly covered with sterile gauze. For the (III) treatment group, 25 μL of CIL@ICG/PFH@O_2 solution (100 μg mL^{-1}) was added and covered with sterile gauze. For the (IV) treatment group, 25 μL of CIL@ICG/PFH@O_2 solution (100 μg mL^{-1}) was added and irradiated with 808 nm NIR (1 W cm^{-2}) for 10 min before being covered with sterile gauze. The wound area of different treatment groups was recorded every two days, and the wound area was measured by using the ImageJ software. On day 3 of treatment, the wound tissues of mice in each group were extracted and stained with hematoxylin–eosin (H&E). Moreover, the antibacterial activities of different materials were evaluated on day 6. The infected tissue was isolated and homogenized in a PBS solution, and 10 μL diluted solution was plated onto LB agar plates and grown at 37 °C overnight, and colonies grown on the plates were counted for analysis.

Data availability

The datasets supporting this article have been uploaded as part of this manuscript and its corresponding ESI.†

Author contributions

F. Y. and J. G. conceived and designed the project. J. Z. synthesized and fully characterized all materials. W. W. and Z. Z. completed the animal experiments together. Q. Z. provided some starting materials and assisted with the data analysis. F. Y., J. G. and J. Z. drafted the manuscript. All authors have discussed the results and given approval to the manuscript.

Conflicts of interest

The authors declare no conflict of interest.

Acknowledgements

This work was supported by the National Natural Science Foundation of China (No. 21835005 and U1862109), Science and Technology Development Plan Project of Suzhou (SNG2021011), Livelihood Technology Project of Suzhou (SKJY2021042), Collaborative Innovation Center of Suzhou

Nano Science and Technology, and the Project funded by the Priority Academic Program Development of Jiangsu Higher Education Institutions.

References

1 Z. Luo, H. Cui, J. Guo, J. Yao, X. Fang, F. Yan, B. Wang and H. Mao, *Adv. Funct. Mater.*, 2021, **31**, 2100336.
2 A. E. Clatworthy, E. Pierson and D. T. Hung, *Nat. Chem. Biol.*, 2007, **3**, 541–548.
3 L. S. J. Roope, R. D. Smith, K. B. Pouwels, J. Buchanan, L. Abel, P. Eibich, C. C. Butler, P. S. Tan, A. Sarah Walker, J. V. Robotham and S. Wordsworth, *Science*, 2019, **364**, eaau4679.
4 M. van Oosten, M. Hahn, L. M. A. Crane, R. G. Pleijhuis, K. P. Francis, J. M. van Dijl and G. M. van Dam, *FEMS Microbiol. Rev.*, 2015, **39**, 892–916.
5 W. A. Adedeji, *Annals of Ibadan Postgraduate Medicine*, 2016, **14**, 56–57.
6 M. Hutchings, A. Truman and B. Wilkinson, *Curr. Opin. Microbiol.*, 2019, **51**, 72–80.
7 Y. Takahashi and M. Igarashi, *J. Antibiot.*, 2018, **71**, 4–14.
8 P. Domingo-Calap and J. Delgado-Martínez, *Antibiotics*, 2018, **7**, 66.
9 C. T. Kåhrström, *Nat. Rev. Microbiol.*, 2013, **11**, 146.
10 J. Sun, L. Song, Y. Fan, L. Tian, S. Luan, S. Niu, L. Ren, W. Ming and J. Zhao, *ACS Appl. Mater. Interfaces*, 2019, **11**, 26581–26589.
11 W. Wang, C. Zhang, M. Zhang, P. Pei, W. Zhou, Z. Zha, M. Shao and H. Qian, *Chem. Eng. J.*, 2020, **381**, 122630.
12 N. O. May Andoy, K. Jeon, C. Titus Kreis, R. A. May Sullan, N. M. O Andoy, K. Jeon, C. T. Kreis and R. M. A. Sullan, *Adv. Funct. Mater.*, 2020, **30**, 2004503.
13 J. Li, S. Song, J. Meng, L. Tan, X. Liu, Y. Zheng, Z. Li, K. W. K. Yeung, Z. Cui, Y. Liang, S. Zhu, X. Zhang and S. Wu, *J. Am. Chem. Soc.*, 2021, **143**, 15427–15439.
14 M. Xu, L. Li and Q. Hu, *Biomater. Sci.*, 2021, **9**, 1995–2008.
15 E. Lee, X. Li, J. Oh, N. Kwon, G. Kim, D. Kim and J. Yoon, *Chem. Sci.*, 2020, **11**, 5735–5739.
16 M. Ma, N. Gao, X. Li, Z. Liu, Z. Pi, X. Du, J. Ren and X. Qu, *ACS Nano*, 2020, **14**, 9894–9903.
17 X. Wang, F. Lv, T. Li, Y. Han, Z. Yi, M. Liu, J. Chang and C. Wu, *ACS Nano*, 2017, **11**, 11337–11349.
18 B. Liu, C. Li, P. Yang, Z. Hou, J. Lin, B. Liu, Z. Hou, J. Lin, C. Li and P. Yang, *Adv. Mater.*, 2017, **29**, 1605434.
19 D. Hu, H. Li, B. Wang, Z. Ye, W. Lei, F. Jia, Q. Jin, K. F. Ren and J. Ji, *ACS Nano*, 2017, **11**, 9330–9339.
20 Y. Liu, Z. Guo, F. Li, Y. Xiao, Y. Zhang, T. Bu, P. Jia, T. Zhe and L. Wang, *ACS Appl. Mater. Interfaces*, 2019, **11**, 31649–31660.
21 W. Qian, C. Yan, D. He, Y. Yu, L. Yuan, M. Liu, G. Luo and J. Deng, *Acta Biomater.*, 2018, **69**, 256–264.
22 Z. Liu, X. Zhao, B. Yu, N. Zhao, C. Zhang and F. J. Xu, *ACS Nano*, 2021, **15**, 7482–7490.
23 Z. H. Yu, X. Li, F. Xu, X. Le Hu, J. Yan, N. Kwon, G. R. Chen, T. Tang, X. Dong, Y. Mai, D. Chen, J. Yoon, X. P. He and H. Tian, *Angew. Chem., Int. Ed.*, 2020, **59**, 3658–3664.
24 J. Feng, W. Yu, Z. Xua and F. Wang, *Chem. Sci.*, 2020, **11**, 1649–1656.
25 A. Maleki, J. He, S. Bochani, V. Nosrati, M.-A. Shahbazi and B. Guo, *ACS Nano*, 2021, **15**, 18895–18930.
26 L. A. Ortiz-Rodríguez and C. E. Crespo-Hernández, *Chem. Sci.*, 2020, **11**, 11113–11123.
27 S. Liu, G. Feng, B. Z. Tang and B. Liu, *Chem. Sci.*, 2021, **12**, 6488–6506.
28 L. Pan, J. Liu and J. Shi, *Adv. Funct. Mater.*, 2014, **24**, 7318–7327.
29 C. Zheng, M. Zheng, P. Gong, D. Jia, P. Zhang, B. Shi, Z. Sheng, Y. Ma and L. Cai, *Biomaterials*, 2012, **33**, 5603–5609.
30 H. Fan, Y. Fan, W. Du, R. Cai, X. Gao, X. Liu, H. Wang, L. Wang and X. Wu, *Nanoscale*, 2020, **12**, 9517–9523.
31 X. Wang, Y. Yu, K. Cheng, W. Yang, Y. Liu and H. Peng, *Microchim. Acta*, 2019, **186**, 1.
32 K. Deng, Z. Hou, X. Deng, P. Yang, C. Li and J. Lin, *Adv. Funct. Mater.*, 2015, **25**, 7280–7290.
33 Y. Wu, Z. Chen, Z. Yao, K. Zhao, F. Shao, J. Su and S. Liu, *Adv. Funct. Mater.*, 2021, **31**, 2104643.
34 H. Zhou, M. Guo, J. Li, F. Qin, Y. Wang, T. Liu, J. Liu, Z. F. Sabet, Y. Wang, Y. Liu, Q. Huo and C. Chen, *J. Am. Chem. Soc.*, 2021, **143**, 1846–1853.
35 J. Wang, L. Liu, Q. You, Y. Song, Q. Sun, Y. Wang, Y. Cheng, F. Tan and N. Li, *Theranostics*, 2018, **8**, 955–971.
36 H. Y. Lee, H. W. Kim, J. H. Lee and S. H. Oh, *Biomaterials*, 2015, **53**, 583–591.
37 L. Zhang, H. Qin, F. Zeng, Z. Wu, L. Wu, S. Zhao and D. Xing, *Nanoscale*, 2020, **12**, 16034–16040.
38 Y. Zhou, Z. Wang, Y. Chen, H. Shen, Z. Luo, A. Li, Q. Wang, H. Ran, P. Li, W. Song, Z. Yang, H. Chen, Z. Wang, G. Lu and Y. Zheng, *Adv. Mater.*, 2013, **25**, 4123–4130.
39 J. Fuchs and J. Thiele, *Free Radical Biol. Med.*, 1998, **24**, 835–847.
40 D. M. Castilla, Z.-J. Liu and O. C. Velazquez, *Adv. Wound Care*, 2012, **1**, 225–230.
41 Y. Fang, D. Gu, Y. Zou, Z. Wu, F. Li, R. Che, Y. Deng, B. Tu and D. Zhao, *Angew. Chem.*, 2010, **122**, 8159–8163.
42 S. Tian, H. Bai, S. Li, Y. Xiao, X. Cui, X. Li, J. Tan, Z. Huang, D. Shen, W. Liu, P. Wang, B. Z. Tang and C. Lee, *Angew. Chem., Int. Ed.*, 2021, **133**, 11864–11868.
43 S. Chen, B. Huang, W. Pei, L. Wang, Y. Xu and C. Niu, *Int. J. Nanomed.*, 2020, **15**, 8641–8658.
44 P. Cabrales and M. Intaglietta, *ASAIO J.*, 2013, **59**, 337.
45 M. Wang, J. Shi, H. Mao, Z. Sun, S. Guo, J. Guo and F. Yan, *Biomacromolecules*, 2019, **20**, 3161–3170.
46 J. Shi, M. Wang, Z. Sun, Y. Liu, J. Guo, H. Mao and F. Yan, *Acta Biomater.*, 2019, **97**, 247–259.
47 L. Li, L. Cao, X. Xiang, X. Wu, L. Ma, F. Chen, S. Cao, C. Cheng, D. Deng and L. Qiu, *Adv. Funct. Mater.*, 2021, 2107530.
48 Q. Wu, G. Wei, Z. Xu, J. Han, J. Xi, L. Fan and L. Gao, *ACS Appl. Mater. Interfaces*, 2018, **10**, 25026–25036.
49 Z. Zhou, B. Zhang, H. Wang, A. Yuan, Y. Hu and J. Wu, *Theranostics*, 2018, **8**, 4898–4911.

50 C. Zhang, W. Chen, L. Liu, W. Qiu, W. Yu and X. Zhang, *Adv. Funct. Mater.*, 2017, **27**, 1700626.
51 C. Zhang, J. Guo, X. Zou, S. Guo, Y. Guo, R. Shi and F. Yan, *Adv. Healthcare Mater.*, 2021, **10**, 2100775.
52 R. Kannan, P. Prabakaran, R. Basu, C. Pindi, S. Senapati, V. Muthuvijayan and E. Prasad, *ACS Appl. Bio Mater.*, 2019, **2**, 3212–3224.
53 G. T. Spence, C. Chan, F. Szemes and P. D. Beer, *Dalton Trans.*, 2012, **41**, 13474–13485.
54 L. Zhou, K. Dong, Z. Chen, J. Ren and X. Qu, *Carbon*, 2015, **82**, 479–488.
55 G. Song, C. Ji, C. Liang, X. Song, X. Yi, Z. Dong, K. Yang and Z. Liu, *Biomaterials*, 2017, **112**, 257–263.